1 **Impacts of anomalies in Arctic sea ice outflow on sea ice in the Barents and Greenland**

2 **Seas during the winter-to-summer seasons of 2020**

3 Fanyi Zhang[1,2], Ruibo Lei[2,1]*, Xiaoping Pang[1], Mengxi Zhai[2], Na Li[2]

4 [1]Chinese Antarctic Center of Surveying and Mapping, Wuhan University, Wuhan 430079, China

5 [2]Key Laboratory for Polar Science of the MNR, Polar Research Institute of China, Shanghai 200136, China

6 *Correspondence to:* Ruibo Lei（leiruibo@pric.org.cn.)

7 **Abstract:** Arctic sea ice outflow to the Atlantic Ocean is essential to Arctic sea ice mass loss and the hydrographical and

8 ecological environments in the Barents and Greenland Seas (BGS). In the context of the extremely positive Arctic Oscillation

9 (AO) in January–March 2020, the impacts and feedback mechanisms on a seasonal scale of anomalies in Arctic sea ice outflow

10 on winter–spring sea ice and other marine environmental conditions in the subsequent months until early summer in the BGS

11 were investigated. The results reveal that the total sea ice area flux (SIAF) through the Fram Strait, the Svalbard-Franz Josef

12 Land, and the Franz Josef Land-Novaya Zemlya passageways in January–March and June 2020 were higher than the 1988–

13 2020 climatology, mainly through the Fram Strait (77.6%). The interannual variability of this total SIAF was dominated by

14 changes in ice motion speed ($R = +0.86$, $P < 0.001$). The relatively high ice speed along the Transpolar Drift in January–June

15 2020 was related to the positive phases of winter (JFM) AO and the winter-spring air pressure gradient across the western and

16 eastern Arctic Ocean. The abnormally high Arctic sea ice outflow led to an increased sea ice area and thickness in the BGS,

17 which has been observed since March 2020, especially in May–June. In this region, the April sea ice area was significantly

18 negatively correlated with synchronous sea surface temperature (SST) as well as the lagging SST of 1–3 months. High sea ice

19 area in spring (AMJ) 2020 also inhibited phytoplankton bloom, with an extremely low *Chlorophyll-a* concentration observed

20 over the BGS in April. Therefore, this study suggests that winter–spring Arctic sea ice outflow can be considered as a predictor

21 of changes in sea ice and other marine environmental conditions in the BGS in the subsequent months, at least until early

22 summer. The results increase our understanding of the physical connection between the central Arctic Ocean and the peripheral

23 seas.

24 **KEYWORDS**: Arctic Ocean; Sea ice; Transpolar Drift; Atmospheric circulation pattern; Barents Sea; Greenland Sea

25

1. Introduction

Arctic sea ice has been experiencing a dramatic loss over the past four decades, and the overall decline in sea ice extent is statistically significant in all seasons (Cavalieri and Parkinson, 2012). In winter, due to the absence of land constraints, reductions in the Arctic sea ice extent occurred mainly in the peripheral seas, particularly in the Barents and Greenland Seas (BGS). From 1979 to 2016, sea ice changes in the Barents and Greenland Seas accounted for 27% and 23% of the total Arctic sea ice extent loss in March, respectively (Onarheim et al., 2018). Changes in Arctic sea ice may have potentially far-reaching effects not only on Arctic local climate and ecological environments but also on extreme weather or climatic events at lower latitudes (Schlichtholz, 2019). Previous studies have revealed the relations of Eurasian winter cold anomalies to sea ice reduction in the Barents Sea (e.g., Mori et al., 2014).

Through the regulations of thermodynamic and dynamic processes, large-scale atmospheric circulation patterns have significant implications on sea ice growth and decay, as well as advection and spatial redistribution (Frey et al., 2015; Dorr et al., 2021; Dethloff et al., 2022). Dynamically, enhanced wind forcing, associated with anomalous atmospheric circulations, could induce increased sea ice motility and deformation, especially for Arctic sea ice outflow through the Fram Strait (e.g., Cai et al., 2020). Associated with the conveyor belt of the Transpolar Drift (TPD), Arctic sea ice can be exported to the BGS and finally enter the North Atlantic (Kwok, 2009), which is an important mechanism for decreases in the total sea ice volume over the pan-Arctic (Smedsrud et al., 2017), especially for the loss of multi-year ice (Kwok et al., 2009). Moreover, Arctic sea ice advection along the TPD is also capable of transporting ice-rafted materials or extend ice-associated biomes from the Eurasian shelf to the Arctic basin, and eventually out of the Arctic Ocean (Mørk et al., 2011; Peeken et al., 2018; Krumpen et al.,2020). The Arctic sea ice outflow, associated with equivalent fresh water outflow being comparable to that carried by the East Greenland current (Spreen et al., 2009; de Steur et al., 2014), contributed significantly to the formation of deep water in the north of the Atlantic Ocean (Lemke et al., 2000). In turn, the increase in the oceanic heat inflow from the north Atlantic Ocean leads to the Atlantification and promotes the retreat of sea ice in the BGS (Shu et al., 2021).

As the peripheral seas of the Arctic Ocean, the BGS are not completely covered by sea ice even in winter, so the ocean dynamic processes and atmosphere-ocean interactions are relatively strong in this region compared to the central Arctic Ocean (Smedsrud et al., 2013). Sea ice outflow from the Arctic Ocean plays a crucial role in shaping the icescape in this region. And most notably, more marine primary productivities occur in the BGS than in other regions for the waters north of the Arctic Circle due to the supply of nutrients from the south and the availability of more photosynthetic light because of the relatively low sea ice coverage (Arrigo and van Dijken, 2015; Mayot et al., 2020). Naturally, the bloom of primary productivity in this region is greatly affected by the distribution and seasonality of sea ice, mainly by regulating the available photosynthetic light

55 (Wassmann et al., 2010). Thus, further revealing the influence and feedback mechanisms of abnormal Arctic sea ice outflow

56 on the marine environmental conditions in the downstream of TPD over the BGS on a seasonal scale could improve the

57 understanding of the physical connections between the central Arctic Ocean and the BGS, which is still not particularly clear,

58 especially in conjunction with some extreme atmospheric circulation events.

59 Variations in Arctic sea ice outflow to the BGS are associated with a variety of large-scale atmospheric circulation patterns

60 and local synoptic events (Bi et al., 2016), among which the atmospheric circulation patterns of the Arctic Oscillation (AO)

61 (Kwok, 2009) and the Central Arctic west-east air pressure gradient Index (CAI; Vihma et al., 2012) can play significant roles.

62 The AO index is the dominant pattern of surface mean air pressure anomalies, with a positive AO index indicating below

63 normal air pressure in the Arctic and above normal over external regions (Dethloff et al., 2022). When the AO is in a relatively

64 extreme positive phase, the westward shift of the TPD allows thicker multi-year ice to be advected from the central Arctic

65 Ocean towards Fram Strait (Rigor et al., 2002). In January–March 2020, the AO experienced an unprecedented positive phase,

66 which led to the relatively rapid southward drift of the ice camp of the Multidisciplinary drifting Observatory for the Study of

67 Arctic Climate (MOSAiC) during the winter and early spring of 2019–2020 (Krumpen et al., 2021). The CAI, on the other

68 hand, represents the east-west gradient of the SLP across the central Arctic Ocean, approximately perpendicular to the TPD

69 (Vihma et al., 2012). Thereby, it can indicate the intensity of TPD to a high degree (Lei et al., 2016), which directly affects the

70 outflow of Arctic sea ice toward the BGS.

71 Thereby, the main objectives of this study are to clarify the effects of atmospheric circulation anomalies on Arctic sea ice

72 outflow during winter–spring 2020, and their effects on sea ice distributions and other marine conditions over the BGS in the

73 subsequent months until early summer, in order to reveal seasonal impacts and feedback mechanisms. The sections of this

74 paper are organized as follows. The datasets used to measure anomalies in atmospheric, sea ice, and oceanic conditions are

75 briefly described in Section 2. Section 3 presents the anomalies in atmospheric circulation and Arctic sea ice outflow in the

76 study year, as well as their influences on sea ice conditions in the BGS. Links of Arctic sea ice outflow to atmospheric

77 circulation, the impact of sea ice anomalies on the hydrographical and ecological conditions in the BGS, and the

78 representativeness of the connections between sea ice anomalies and the marine environments identified in 2020 related to the

79 climatological data, are discussed in Section 4. The conclusions are presented in the last section.

80 **2. Data and methods**

81 **2.1 Study area**

82 Our studies focus on the downstream region of the TPD, i.e., the Barents Sea (72°–80°N, 20°–60°E) and the Greenland

83   Sea (72°–80°N, 20°W–20°E) to assess the impacts of sea ice outflow from the Arctic Ocean on the sea ice and other marine

84   conditions in this region on a seasonal scale. To quantify the sea ice outflow, we calculated the sea ice area flux (SIAF) through

85   the passageways between the Arctic Ocean and the BGS region, i.e., through the Fram Strait, the Svalbard-Franz Josef Land

86   (S-FJL) passageway, and the Franz Josef Land-Novaya Zemlya (FJL-NZ) passageways (Figure 1), with the widths of about

87   448, 284, and 326 km, respectively.

88
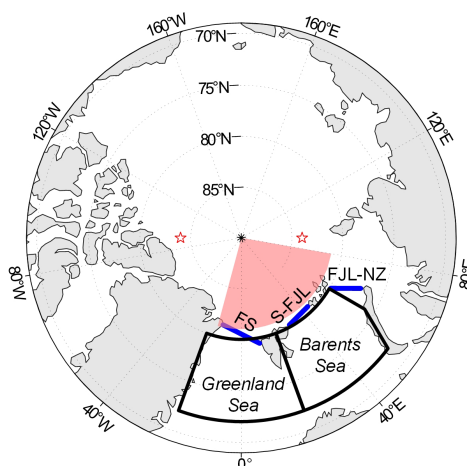
Figure 1. Geographical locations of the Barents and Greenland Seas (black frames). Blue lines represent the passageways defined for the calculations of sea ice area flux. The red stars indicate the locations (90° W, 84° N, and 90° E, 84°N) defined to calculate the Central Arctic west-east air pressure gradient Index (CAI). The Atlantic sector of TPD is shaded in red and the sea ice motion speed in this region is used to quantify the link to wind speed.

2.2 Data

94   We used the National Snow and Ice Data Center (NSIDC) Polar Pathfinder version 4 sea ice motion (SIM) vectors and

95   National Oceanic and Atmospheric Administration (NOAA)/NSIDC Climate Data Record passive microwave sea ice

96   concentration version 4 (SIC) (Tschudi et al., 2019; Meier et al., 2021) to calculate the SIAF from the Arctic Ocean to the BGS.

97   The choice of this SIM product was motivated by its spatial completeness and temporal continuance. The SIM product is the

98   most optimal interpolation merged result using satellite remote sensing data, buoy observations, and reanalyzed wind data

99   (Tschudi et al., 2020). This product provides daily ice drift components georeferenced to the Equal-Area Scalable Earth Grid

100   (EASE-Grid) with a spatial resolution of 25 km. The SIC product was a rule-based combination of SIC estimates from the

101   National Aeronautics and Space Administration (NASA) Team (NT) algorithm (Cavalieri et al., 1984) and NASA Bootstrap

102   (BT) algorithm (Comiso, 1986), derived from the Scanning Multichannel Microwave Radiometer (SMMR), Special Sensor

103   Microwave Imager (SSM/I), and Special Sensor Microwave Imager/Sounder (SSMIS) radiometers. Daily SIC fields were

104   gridded on a 25-km resolution polar stereographic grid. Both datasets are available from October 1978 to the present. However,

105   there is a gap in the SIC dataset from 3 December 1987 through 12 January 1988. The sea ice area (SIA) was defined as the

106   cumulative area of the waters covered by sea ice with the SIC above 15%. For the study region, we used the SIC data since

107   1979 to estimate the SIA abnormal from January to June in the study year of 2020. In addition, we used data from the NSIDC

108   Sea Ice Index version 3 (Fetterer et al., 2017) to obtain monthly SIA changes in the Northern Hemisphere in 2020.

109   The sea ice thickness (SIT) data used to characterize the sea ice conditions in the study region was mainly derived from

110   satellite remote-sensed observations, and supplemented by the modeling product in early summer. The remote-sensed SIT data

111   was created from the merged CryoSat-2 and Soil Moisture and Ocean Salinity (SMOS) observations, hereinafter referred to as

112   CryoSat-2/SMOS (Ricker et al., 2017). The CryoSat-2/SMOS dataset makes full use of the detectability of SMOS for thin sea

113   ice (<1.0 m) and the measurement capability of CryoSat-2 for thicker sea ice, which ensures obtaining a more comprehensive

114   product of SIT. Weekly CryoSat-2/SMOS SIT data were available on a 25-km EASE-Grid during the freezing season of

115   October to mid-April from 2010 to the present. During the ice melt season from May–June, we used the monthly SIT modeling

116   product obtained from the Pan-Arctic Ice Ocean Modeling and Assimilation System (PIOMAS; Zhang and Rothrock, 2003).

117   The PIOMAS is a coupled ice-ocean model assimilation system that has been extensively validated and compared with satellite,

118   submarine, airborne, and in situ observations, which has proved it can reproduce the observed sea ice thickness well (Zhang

119   and Rothrock, 2003; Schweiger et al., 2011; Stroeve et al., 2014; Wang et al., 2016). The monthly PIOMAS SIT is gridded on

120   a generalized orthogonal curvilinear coordinate system with an average resolution of 22 km. We regridded the monthly SIT

121   data on the 25-km EASE-Grid to maintain consistency with the CryoSat-2/SMOS SIT data. Here, we used the CryoSat-

122   2/SMOS SIT from December to April, and the PIOMAS SIT from May to June in 2011–2020 to estimate the anomaly in SIT

123   during the study year of 2020.

124   Sea surface temperature (SST) and *Chlorophyll-a* (*Chl-a*) could be used as the best proxies to indicate the physical state

125   and primary productivity over a basin scale (Siswanto, 2020), and can be easily obtained from satellite remote sensing. Thus,

126   we used these two variables for the period 2005–2020 to characterize the anomalies in the hydrographical and ecological

127   conditions over the BGS during the study year, respectively. The SST data was obtained from NOAA Daily Optimum

128   Interpolation SST High Resolution dataset version 2, which assimilated buoy and ship-based data, satellite SST data, and proxy

129   SST data in the ice-covered regions of the Arctic (Reynolds et al., 2007). This dataset is available on a regular grid of

130   0.25°×0.25°. The merged *Chl-a* ocean colour product is available from the Ocean Colour-Climate Change Initiative (OC-CCI)

131   project, which is derived from multiple ocean colour sensors (Sathyendranath et al., 2021). The *Chl-a* dataset has a monthly

132   temporal resolution and a spatial resolution of 4 km.

133 The fifth generation reanalysis ERA5 datasets from European Centre for Medium-range Weather Forecasts (ECMWF)

134 provide sea level pressure (SLP), 2-m air temperature, 10-m surface wind, as well as surface net heat fluxes of longwave

135 radiation, shortwave radiation, sensible heat, and latent heat (Hersbach et al., 2020). These variables, with about 30-km

136 horizontal and 1-h temporal resolutions, were used to identify anomalies in surface atmospheric conditions or forcing over the

137 study region. The ERA5 reanalysis uses a significantly more advanced 4D-var assimilation scheme, with improved

138 performance over the Arctic compared to ERA-Interim (Graham et al., 2019). We used the monthly AO index provided by

139 NOAA Climate Prediction Center (CPC), which was constructed by projecting a daily 1000 hPa height anomaly at the 20°N

140 poles onto the AO loading pattern (Thompson and Wallace, 1998). In addition, the hourly SLP data from the ERA5 reanalysis

141 were used to calculate the monthly CAI, defined as the difference between SLPs at 90° W, 84° N, and 90° E, 84°N.

142 **2.3 Methods**

143 The SIAF was defined as the magnitude of the SIA conveyed through a defined gate during a given period. According to

144 Kwok (2009), we estimated the monthly SIAF by accumulating the daily integral of the products between the gate-

145 perpendicular component of the SIM and SIC along the defined passageways. Positive (negative) values correspond to the

146 southward (northward) SIAF. Prior to the estimation of SIAF, we interpolated the SIC into the SIM projection and retrieved

147 the gate-perpendicular SIM components. According to the trapezoidal rule, the SIAF was estimated as follows:

148 $SIAF = \sum_{i=1}^{n} u_i C_i \Delta x$ (1)

149 where n is the number of points along the passageway, u_i is the gate-perpendicular SIM component, C_i is the SIC at the

150 ith grid cell, and Δx is the width of a grid cell (25km).

151 The corresponding error of SIAF depends on the uncertainties of SIM and SIC products, the sampling number along the

152 passageways, and the calculation period. For daily SIM vectors, the error was estimated to be about 4.1 km·day^{-1} (Tschudi et

153 al., 2019). Several assessments indicated an accuracy of about 5% in SIC fields (Peng et al., 2013). Assuming that these two

154 sources of error are independent, the uncertainty (σ_f) in estimating SIAF across a 1-km wide gate was estimated at about 2.92,

155 3.80, and 2.68 km^2·day^{-1} for the Fram Strait, S-FJL, and FJL-NZ, respectively. If we assume that the errors of the samples are

156 additive, unbiased, uncorrelated, and normally distributed, the uncertainty in daily SIAF is $\sigma_D = \sigma_f L / \sqrt{N_s}$ (Kwok, 2009),

157 where L is the length of the gate, and N_s is the number of independent samples across the gate. From January to June, the

158 monthly average uncertainties in SIAF through three passageways were estimated to be approximately 1.81×10^3 to 1.96×10^3

159 km^2, which were about 3.7%–13.9% of the monthly magnitude and therefore considered acceptable.

160 To describe the relationship between the SIAF and the sea ice transport before reaching the defined passageway, we also

161   restructured the sea ice backward drift trajectories from the defined passageways (Fram Strait, S-FJL, and FJL-NZ) over the

162   three defined periods of January–April, January–May, and January–June 2020, with the ice drifting from the north since 1

163   January into the passageways by 30 April, 31 May, and 30 June, respectively. The adoption of three periods to restructure the

164   ice backward drift trajectories is conducive to further distinguishing the difference between the anomalies over the winter

165   (JFM) or the period of winter through spring (AMJ). In addition, the restructured backward trajectory of sea ice from the

166   defined passageway can help to identify the source area of the ice, thus reflecting the relationship between the sea ice outflow

167   and the sea ice conditions in the source area. The sea ice backward drift trajectories were restructured according to Lei et al.

168   (2019), and the zonal (X) and meridional (Y) coordinates of the backward ice trajectories were calculated as follows:

169    $X(t) = X(t-1) + U(t-1) \cdot \delta_t$ (2)

170   and $Y(t) = Y(t-1) + V(t-1) \cdot \delta_t$ (3)

171   where $U(t)$ and $V(t)$ are the ice motion components at the time t along the ice trajectories and the δ_t is the calculation

172   time step of –1 day. Thereby, the course of time corresponding to the sea ice backward drift trajectory is reversed from the

173   defined date to 1 January.

174   In order to reveal the contribution of surface heat budget to sea ice melting, we calculated the potential change in SIT

175   ($\triangle h$) over the time of $\triangle t$, associated with anomalies in surface net heat fluxes over the BGS, according to Parkinson and

176   Washington (1979):

177    $-\Delta h = \frac{\triangle t}{\rho L} [\delta FL_{w\downarrow} + \delta FS_{w\downarrow} + \delta H_{\downarrow} + \delta LE_{\downarrow}]$ (4)

178   where ρ is the density of sea ice (917 kg·m^{-3}), L is the latent heat of fusion for sea ice (333.4 kJ·kg^{-1}), $\delta FL_{w\downarrow}$, $\delta FS_{w\downarrow}$, $\delta H_{\downarrow}$

179   and $\delta LE_{\downarrow}$ represent the anomalies in surface net fluxes of longwave radiation, shortwave radiation, sensible heat, and latent

180   heat, respectively, with the positive value denoting the downward heat flux. We note that, the Eq. 4 focuses on the atmosphere-

181   to-ice heat fluxes but ignores the effects of ocean heat flux. Thus, it can only be used to assess the impact of atmospheric

182   anomaly on the local sea ice mass balance.

183   **3. Results**

184   **3.1 Anomalies in atmospheric circulation patterns**

185   As shown in Table 1, the monthly AO was in an unusually positive phase from January to March 2020, with the values

186   maintaining the top three among the years of 1979–2020. And then, the AO decreased to a smaller value in April and turned

187 to a weakly negative phase in May–June 2020. Monthly CAI in January–June 2020 experienced a continuous positive phase

188 with an average CAI of 8.5 hPa, which was the largest in 1979–2020. During winter–spring 2020, there were two peaks of

189 monthly CAI occurring in March and June, with the values of first and fourth in 1979–2020, respectively.

190   In January–March 2020, accompanied by an unusual positive phase of the AO, the entire Arctic Ocean was almost

191 dominated by abnormally low SLP compared to the 1979–2020 climatology (the first column of Figure 2). In January 2020, a

192 large-scale anomalous low SLP appeared near the Kara Sea, and the high-pressure center was observed in Northern North

193 America. This SLP pattern induced a positive CAI and northerly winds from the high Arctic towards the Barents Sea,

194 accelerating the southward drift of Arctic sea ice into the Barents Sea and causing regional negative air temperature anomalies

195 there. In February 2020, the abnormally low SLP dominated near the Barents and Kara Seas, inducing strong northerly winds

196 in the Atlantic sector of the Arctic Ocean. This SLP pattern continued to cause abnormally high wind speeds over the Atlantic

197 sector of TPD region, further promoting Arctic sea ice advecting into the BGS and keeping the negative air temperature

198 anomalies in this region. In March 2020, the low SLP anomalies moved deeper into the central Arctic Ocean and induced

199 westerly wind anomalies in the BGS.

200   In April 2020, the low SLP in the Arctic, centered in the northern Beaufort Sea, caused the sea ice to continue to advect

201 toward the Barents Sea. Subsequently, the SLP structure over the Arctic Ocean has changed greatly in May 2020, with high-

202 pressure anomalies observed in the Beaufort Sea. The SLP structure in May 2020 was further conducive to Arctic sea ice

203 advection towards northeastern Greenland. This large change in SLP structure led to the prominently enhanced positive CAI,

204 which reached the second peak in June, even the AO index decreased remarkably during this period (Table 1). Therefore, the

205 AO mainly manifests the SLP structure of the pan-Arctic, regulating the sea ice outflow from the TPD region to the BGS by

206 changing the axis alignment of the TPD. While the CAI mainly affects the wind forcing and ice speed in the TPD region,

207 especially for the Atlantic sector.

208 **Table 1.** Monthly AO Index and CAI in winter–spring 2020 and their ranking in 1979–2020

209
210

	January	February	March	April	May	June
AO	2.419	3.417	2.641	0.928	–0.027	–0.122
Rank	3rd	1st	2nd	7th	23th	26th
CAI/ hPa	4.219	11.317	19.671	5.387	2.219	7.942
Rank	11th	2nd	1st	19th	24th	4th
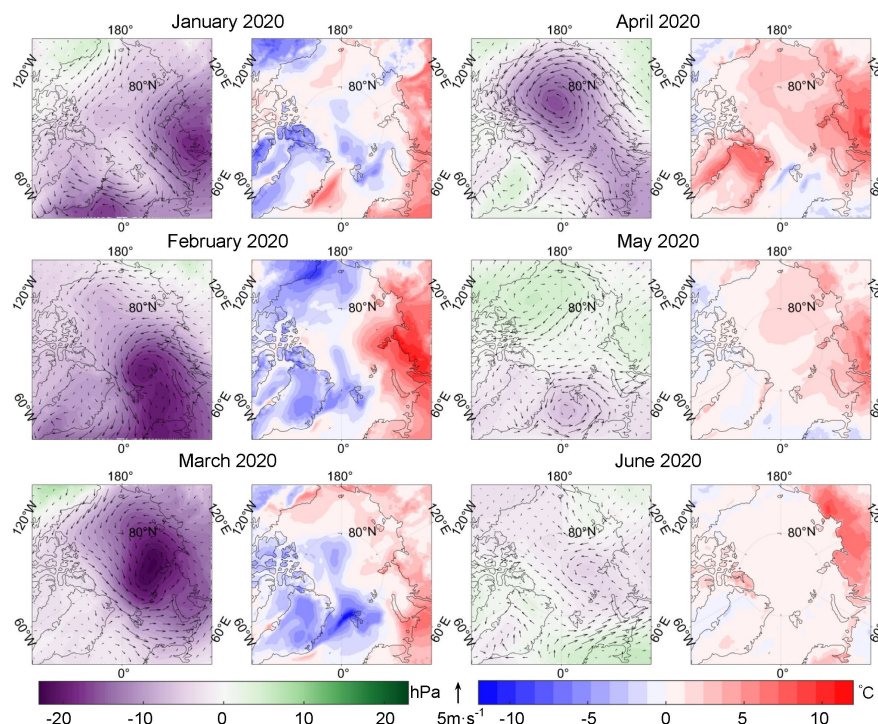
Figure 2. Monthly mean SLP (shading) and 10-m surface wind (arrows) anomalies (the first and third columns), and 2-m air temperature anomalies (the second and fourth columns), during January–June 2020 relative to the 1979–2020 climatology.

### 3.2 Anomalies in Arctic sea ice outflow

We described the SIAF anomalies relative to the 1988–2020 climatology (Figure 3) because differences in satellite data sources could lead to relatively low SIM speeds derived from the SMMR 37-GHz data during 1979–1987 compared to that derived from daily SSM/I 85 GHz data, SSMIS 91 GHz and/or AMSR-E 89 GHz observations in the later years (Kwok, 2009). The cumulative SIAF through Fram Strait and S-FJL both exhibited positive anomalies from January to June 2020. In winter (JFM) 2020, the cumulative SIAF through the Fram Strait was 1.19×10^5 km^2, which was about 1.2 times the 1988–2020 average, and was the second largest in 2010–2020. Especially in March, the monthly SIAF through the Fram Strait (5.77×10^4 km^2) reached the second largest in 1988–2020. The winter cumulative SIAF through the S-FJL in 2020 (1.51×10^4 km^2) also ranked the second largest in 2010–2020. However, the winter cumulative SIAF through the FJL-NZ in 2020 (2.76×10^4 km^2) was only about 81.0% of the 1988–2020 average. This suggests that the sea ice outflow through the FJL-NZ was not sensitive to the atmospheric circulation pattern of extreme positive AO in winter 2020.

In spring (AMJ) 2020, the cumulative SIAF through the Fram Strait was still at an above-average level, especially with positive monthly SIAF anomalies in May–June. However, the spring cumulative SIAF through the S-FJL and FJL-NZ was

The Cryosphere
Discussions

227   only 67.5% and 14.1% of the 1988–2020 average, respectively. This implies that the SIAF through these two passageways,

228   especially for the FJL-NZ passageway in the east, was insensitive to the influence of positive CAI in spring 2020. Consequently,

229   in January–June 2020, the Fram Strait was the main passageway contributing to the abnormally high total sea ice outflow from

230   the Arctic Ocean to the BGS, with relative contributions of 73.3% in winter and 86.7% in spring, respectively, responding to

231   the extreme positive phase of winter AO and the continuous positive phase of winter–spring CAI. In general, in January–

232   March and June 2020, the accumulated SIAF across three passageways was at the above-average level, with the largest positive

233   anomalies occurring in March 2020. The abnormally large Arctic sea ice outflow in winter–spring 2020 subsequently

234   contributed to the dramatic Arctic sea ice loss, resulting in relatively low SIAs of 8.41×10^6 km^2 in June and 5.07×10^6 km^2 in

235   July 2020, ranking the third and first smallest in 1979–2020, respectively.

236   The 1988–2020 data has also revealed that the accumulated SIAF through three passageways in both winter and spring

237   was mainly determined by the SIM speed perpendicular to the passageways ($R = +0.86, +0.85$, respectively; $P < 0.001$). And

238   in January–February, April and June, the SIM speed in the Atlantic sector of TPD was significantly and positively correlated

239   with the wind speed (Table A1). Therefore, under the regulation of positive winter AO and winter–spring CAI in 2020, the

240   relatively high wind speeds led to the larger SIM speeds along the TPD and the increased Arctic sea ice outflow, majorly

241   through the Fram Strait (Figure 3).

242
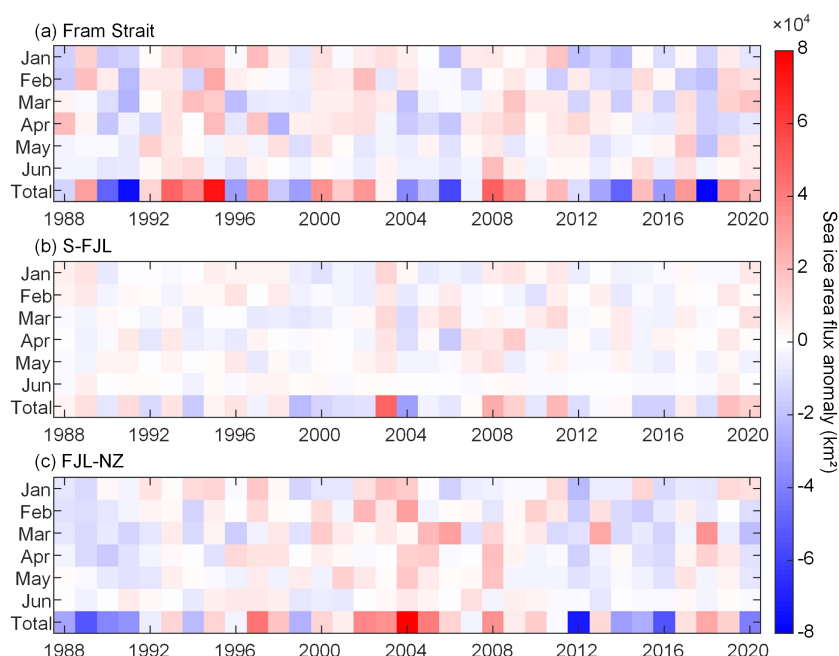
243   **Figure 3.** Monthly anomalies of sea ice area flux (SIAF) through the Fram Strait, S-FJL, and FJL-NZ from 1988 to 2020. The last row of

244   each panel represents the anomalies of cumulative SIAF from January to June.

3.3 Anomalies in sea ice backward trajectories from the passageways

The backward trajectories can be traced back to the original location of sea ice, thereby denoting the source region of sea ice that advected to the passageways. The broader distribution of the sea ice original area implies that more ice would enter the passageways, leading to an increased sea ice outflow. Compared to the sea ice backward trajectories reconstructed using the average SIM vector of 1988–2020 (Figure 4d–4f), the sea ice backward trajectories from the Fram Strait in 2020 were tilted westward (Figure 4a–4c). This implies that the orientation of TPD was more favorable for exporting thicker ice from the western Arctic Ocean and northern Greenland to the Fram strait during winter–spring 2020. Thus, the anomalies of sea ice volume outflow in winter–spring 2020 were expected more obvious than the SIAF anomalies, if considering that the source region of sea ice was generally dominated by relatively thick sea ice. For the Fram Strait, the endpoints of the sea ice backward trajectories were concentrated at 87°–90°N, which indicates that most of the sea ice advected into this passageway was from the region close to the North Pole. It is worth mentioning that, the restructured sea ice backward trajectory in January–June 2020 was very analogous to that of the MOSAiC ice station (Nicolaus et al., 2021) in the same period, with almost parallel orientation and very close drift distance between them (Figure 4c). Since the slight dislocation was mainly attributed to the inconsistent start point between the reconstructed backward trajectory and the MOSAiC trajectory on 30 June 2020, it increases our confidence in using this method to reconstruct the ice backward trajectories. In all three investigation periods, the net distances from the start points at the defined passageways to the endpoints of the reconstructed ice backward trajectories were the second longest in 1988–2020. In S-FJL, sea ice was mainly advected from the confluence of the Kara Sea and the central Arctic Ocean, and its backward trajectories exhibited a relatively high tortuous feature. However, no reasonable backward trajectories of sea ice could be acquired for the S-FJL passageway according to the temporal starting points of 31 May and 30 June. It was because the relatively low SIC in this region by late spring had restricted the acquisition of valid SIM data. The sea ice advected through the FJL-NZ passageway was mainly from the Kara Sea, which can explain why the change in SIAF through this passageway was insensitive to the changes in the TPD intensity or the CAI pattern.

Overall, compared to the 1988–2020 averages, the sea ice backward trajectories through three defined passageways in winter–spring 2020 were characterized as longer and farther west. Especially, the net distances between the terminal points on 1 January and the starting points from Fram Strait since 30 April, 31 May, and 30 June of each year in 1988–2020 were significantly positively correlated with the corresponding SIAF (R = +0.80, +0.72, +0.75, respectively; $P < 0.001$). Thus, the enhanced sea ice meridional motion along the TPD during January–June 2020 promoted more Arctic sea ice export toward the BGS, which in turn accelerated the reduction of sea ice over the pan Arctic Ocean.
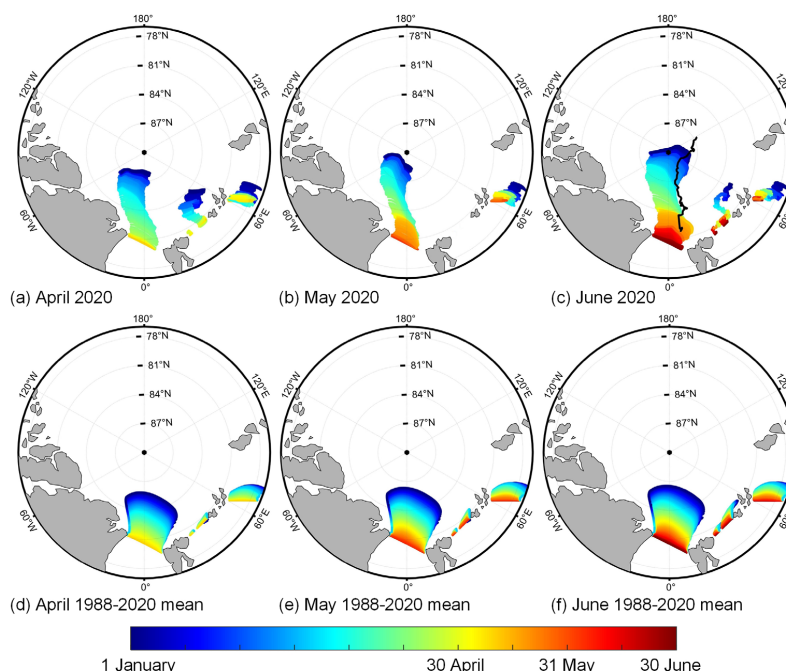
Figure 4. Backward trajectories of sea ice advected to the Fram Strait, S-FJL, and FJL-NZ passageways. The first row shows the backward trajectories of sea ice arriving at the passageways by 30 April, 31 May and 30 June 2020, respectively. The second row is the same as the first row but estimated using the average sea ice motion vector from 1988 to 2020. All endpoints of the reconstructed backward trajectories were set to January 1. The black line in panel (c) represents the MOSAiC trajectories from January 1 to June 30, 2020.

3.4 Anomalies in sea ice area and thickness in the Barents and Greenland Seas

SIA in the BGS generally reaches its annual maximum in April each year, since then, as the air and ocean temperature rises, the SIA begins to decrease. In January–May 2020, the SIA anomalies in the Barents Sea are relatively close to 1979–2020 average (Figure 5) and the SIA maintained the top three values in 2010–2020, indicating that the SIA at the study year was less affected by the significant linear decreasing trend. In the Greenland Sea, the SIA anomalies for April–June 2020 are similar to those in the Barents Sea, with the SIA being the first or second largest in 2010–2020. Consequently, in April–June 2020, the SIA in the BGS was much higher compared to the value after removing the linear decreasing trend from 1979 to 2020. Such a large SIA in the BGS during winter–spring 2020 was linked to a more massive sea ice export from the central Arctic Ocean, because a significant relationship ($R = +0.38$, $P < 0.05$) between the anomalies in Arctic sea ice outflow through the three defined passageways and the SIA in the BGS has been identified based on the 1988–2020 data. However, it is worth noting that the impact of sea ice outflow from the Arctic on the SIA in the BGS would be weakened by local processes, such as heat input from the Atlantic water, which reduces the SIA by promoting sea ice melting in the BGS (Lind et al., 2018).

291   Furthermore, increased sea ice in the BGS, associated with increased subsequent freshwater input to the upper ocean due to

292   ice melting, was conducive to maintaining oceanic stratification, which in turn constitutes feedback and provides favorable

293   conditions for the survival of sea ice.

294
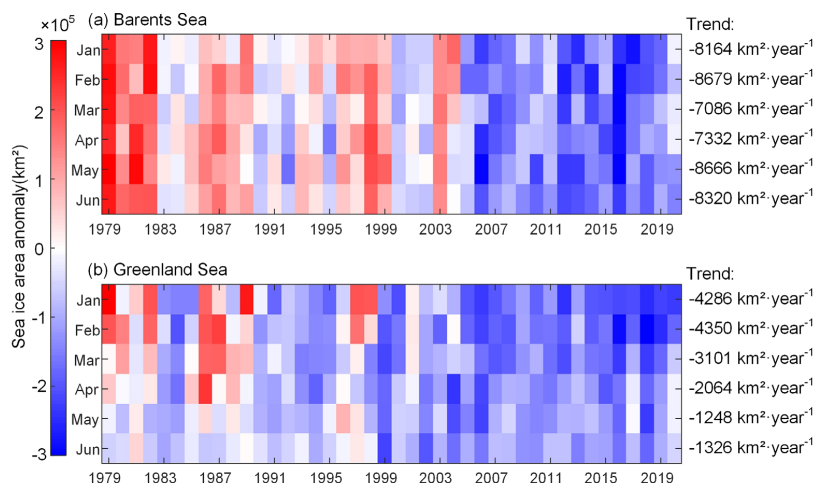
Figure 5. Monthly sea ice area (SIA) anomalies in the Barents and Greenland Seas from 1979 to 2020. Also shown on the right are the
corresponding long-term linear trends, which are all statistically significant at the 0.05 level.

297   As shown in Figure 6, the Greenland Sea initially experienced negative SIT anomalies, and slight positive SIT anomalies

298   were observed in the Barents Sea during December 2019. Since January 2020, more pronounced positive SIT anomalies were

299   observed in the Barents Sea and persisted to June, with the most widespread coverage in April–May. This was related to the

300   anomalous sea ice southward outflow through the S-FJL towards the northern Barents Sea combined with the relatively low

301   local air temperature. In the Greenland Sea, the SIT anomalies in 2020 turned from negative to positive in March and lasted

302   until June. This transition also could be attributed to the remarkably increased Arctic sea ice outflow through the Fram Strait,

303   especially in March 2020.

304   Since sea ice variability is dominated by both local atmospheric and oceanic forcing (Fery et al., 2015), in addition to sea

305   ice inflow due to northerly winds, the persistence of negative air temperature anomalies in the BGS from February to April

306   2020, roughly 2 to 6 °C lower than the 1979–2020 climatology, would also restrict the sea ice melting. Especially in March

307   2020, negative air temperature anomalies covered almost the entire BGS, and the region with the –6 °C anomalies occurred in

308   the coincident region with positive monthly SIT anomalies (Figs. 2 and 6). Moreover, compared to the 1979–2020 climatology,

309   the monthly surface heat fluxes showed upward positive anomalies over the BGS in January–March 2020 (Figure 7), which

310   were mainly dominated by turbulent heat flux (31.3–40.4 W·m^{-2}), accounting for 79.3%–97.1% of the surface heat flux

311   anomalies. Especially, in February and March 2020, the upward anomalies in sensible heat flux were 1.6–2.2 times larger than

312   those in latent heat flux. This was likely due to the relatively large air-sea temperature difference and relatively high wind

313   speed in the BGS during this period, which would result in an unstable atmospheric boundary layer and the increased heat flux

314   from the ocean to the air (Minnett and Key, 2007). In addition to turbulent heat flux, the net longwave radiation revealed

315   relatively small upward anomalies (0.9–8.6 W·m^{-2}) persisting from January to April 2020, which was also favorable for

316   preventing ocean warming and ice melting. From April to June 2020, the monthly anomalies in surface heat fluxes were

317   relatively small, with a value of mostly less than 5 W·m^{-2}. It is worth noting that, upward anomalies in net shortwave radiation

318   were observed in June 2020 over the study region, which coincided with the relatively large SIA and the associated relatively

319   high regional albedo. The anomalies in cumulative surface heat fluxes from January to June 2020 can be related to a reduced

320   decrease of 0.01–0.41 m in SIT, estimated using the Eq. 4. Therefore, in general, the heat exchange between atmosphere and

321   ocean over the BGS, dominated by the upward anomalies in turbulent heat flux in winter 2020, together with the continuous

322   upward anomalies in net longwave radiation during winter and early spring 2020, as well as the upward anomalies in net

323   shortwave radiation in June 2020, was conducive to the survival of sea ice during winter and early summer 2020.
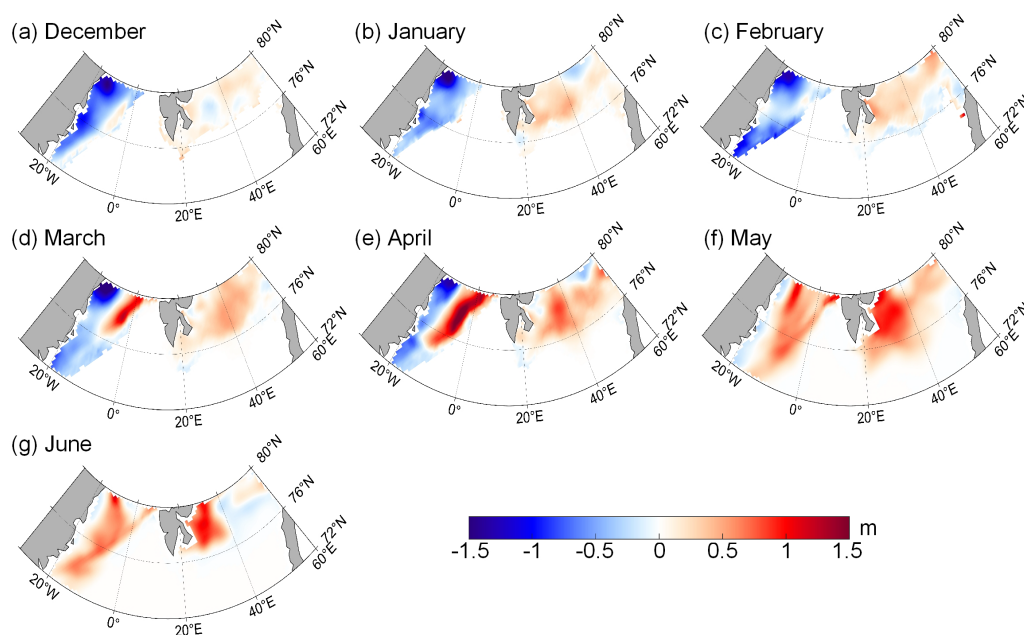
324

325   **Figure 6.** Sea ice thickness (SIT) anomalies in the Barents and Greenland Seas from December 2019 to June 2020 compared to the 2011–

326   2020 average obtained from the CryoSat-2/SMOS product (December–April) and PIOMAS modeled data (May–June).
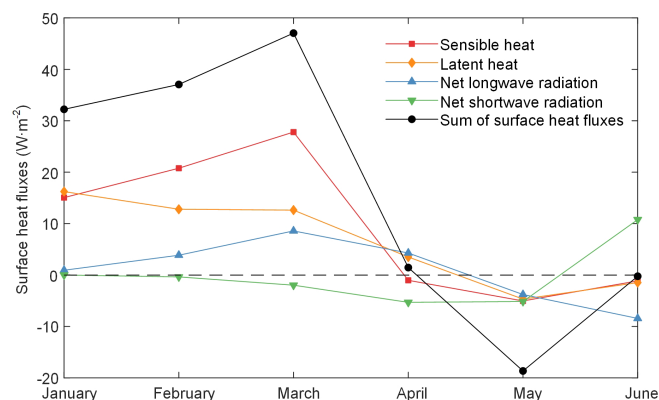
Figure 7. Monthly anomalies in surface heat fluxes of sensible heat, latent heat, net longwave radiation, and net shortwave radiation averaged over the study region from January to June 2020 compared to the 1979–2020 average, with positive values denoting the upward fluxes.

4. Discussion

4.1 Links of Arctic sea ice outflow to atmospheric circulation patterns

In winter–spring 2020, the anomalies in sea ice outflow from the north to the BGS were closely related to the large-scale atmospheric circulation patterns. Furthermore, we quantified the relationship between SIAF and two atmospheric circulation indices (AO and CAI) from 1988 to 2020 to clarify the impact mechanisms of atmospheric circulation on Arctic sea ice outflow. Here, we chose the Fram Strait as the investigated passageway because its SIAF accounts for most (77.6%) of the total SIAF through three passageways. We calculated the correlation coefficient (R) between the detrended monthly SIAF and the detrended AO and CAI from January to June for the period 1988–2020 (Table 2). Since the AO is most active in winter, there is a significant positive correlation between SIAF and the AO in February. This is consistent with Rigor et al. (2002), who revealed that more sea ice advection through the Fram Strait was associated with the high positive winter AO. There is also a significant positive correlation between monthly SIAF and CAI in March–April ($P < 0.05$), which suggests that the relatively high CAI could enhance greater southward advection of Arctic sea ice to the BGS, especially during the period (March–April) with a relatively high ice motion speed in the regions north of the BGS compared to other months (Lei et al., 2016).

Furthermore, we examined the years in which extreme high or low (±1 *standard deviation*) phases of the AO or CAI occurred, based on which we obtained the mean SIM field and reconstructed the sea ice backward drift trajectories during January–June in the corresponding years (Figure A1). Associated with the extreme high phase of AO, the sea ice backward trajectories were almost parallel to the prime meridian, i.e., the orientation of TPD was more westward. It means that the positive phase of AO in winter generally leads to a reduction in the spatial scope of Beaufort Gyre and a westward shift of

348 TPD, which is more conducive to sea ice outflow from the central Arctic Ocean to the BGS (Rigor et al., 2002). Thus, we

349 believe the relationship between the positive phase anomalies of AO and the westward alignment of TPD identified in 2020,

350 as shown in Figure 4, is robust. Whereas the sea ice backward trajectories were further to the east under scenarios with the

351 negative phase of AO. Under the influence of an extremely low AO index, the expanding Beaufort Gyre can weaken the

352 strength of the TPD and reduces Arctic sea ice export (Zhang et al., 2022). Associated with either the positive or negative phase

353 of CAI, the sea ice backward trajectories were similar to those under the corresponding phase of the AO. However, in the two

354 investigated periods of January–May and January–June, there is a higher positive (negative) correlation between the latitude

355 (longitude) of sea ice backward trajectories endpoints and the CAI compared to the AO (Table A2). This relationship was due

356 to the fact that the positive phase of CAI might directly enhance the TPD by strengthening wind forcing, hence favoring sea

357 ice outflow from the central Arctic Ocean into the Fram Strait. The insignificant correlation between them in the investigated

358 period of January–April may be owing to the fact that the sea ice backward trajectories restructured in this period were

359 relatively short range and the variations in the locations of the backward trajectory endpoints between the years were relatively

360 small.

361 **Table 2.** Correlation coefficient (R) between monthly sea ice area flux (SIAF) through the Fram Strait and atmospheric
362 circulation indices in 1988–2020

Month	January	February	March	April	May	June
AO	n.s.	0.437*	n.s.	n.s.	n.s.	n.s.
CAI	0.610***	n.s.	0.403*	0.538**	n.s.	n.s.

363 Note: Significance levels are $P < 0.001$ (***), $P < 0.01$ (**) and $P < 0.05$ (*); n.s. denotes nonsignificance at the 0.05 level.

364 **4.2 Impact of sea ice anomalies on the hydrographical and ecological conditions in the Barents and Greenland Seas**

365 In April–June 2020, the BGS experienced widespread negative anomalies of SST (–1°C to –3 °C), with monthly SSTs being

366 the lowest in 2005–2020 (Figure 8). Furthermore, the small negative SST anomalies over the Barents Sea persisted to August

367 2020. The detrended correlations between the monthly SIA and contemporaneous SST in the BGS from April to June over

368 1982–2020 (Table A3) were significantly negative. The impact and feedback mechanisms can be summarized as that the

369 abnormally large Arctic sea ice outflow in winter–spring 2020 led to an increased SIA and the associated relatively high albedo

370 in the BGS, thereby preventing the absorption of incoming solar radiation by the ocean and suppressing the rise in SST. In

371 turn, relatively colder seawater was not conducive to sea ice melting there. The corresponding correlation coefficients in the

372 Greenland Sea were weaker compared to those in the Barents Sea, which may be due to the relatively complex influence

373 factors on the SST variations in the Greenland Sea. That is to say, the northwestern Greenland Sea is suppressed from cooling

374 effects due to sea ice and surface current inflow from the north, while the southeastern part is subject to warming effects from

375   warm Atlantic heat flow (Wang et al., 2019). Regionally, we found that the negative correlation coefficients between SIA and

376   SST are larger in the southern BGS (76°–80°N) than in the northern part (72°–76°N). This is likely because the SST is more

377   closely correlated with the SIC in areas with less sea ice (Wang et al., 2019). In addition, we examined the statistical

378   relationship between the April SIA and the monthly SST with a lag of 1–3 months in the BGS (Table A4). It manifests that

379   there was a significant negative correlation between them with a lag of 1–2 months, with the decreased correlation coefficients

380   as the increased lagging time. In the Barents Sea, the April SIA still had a significant negative effect on the increase in SST

381   until July, i.e., with a lag of 3 months, whereas in the Greenland Sea, the significant influence of April SIA on the SST only

382   lasted until June. This difference suggests that the sea ice anomalies in the Barents Sea have a longer memory for the impact

383   on the SST than those in the Greenland Sea.
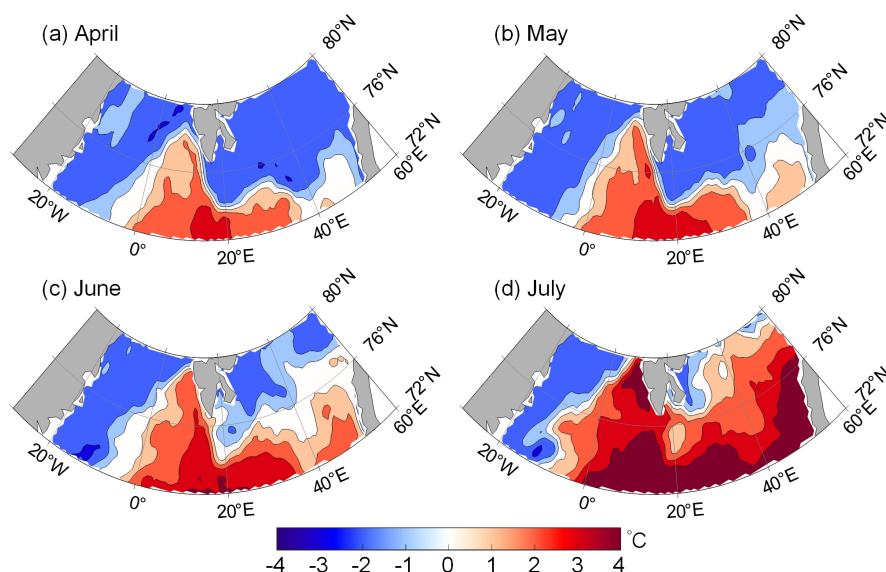
Figure 8. Monthly sea surface temperature (SST) anomalies in the Barents and Greenland Seas from April to July 2020 compared to the 2005–2020 average.

387   Arctic marine primary producers using photosynthetic light during spring bloom are largely restricted by sea ice cover

388   (Campbell et al., 2015). The *Chl-a* over the southern Greenland Sea in April 2020 was smaller compared to the previous 5

389   years. A significant negative correlation between *Chl-a* and SIA in April over 1998–2020 was identified ($R = -0.45$, $P < 0.05$).

390   This implies that the increase in SIA inhibited the growth of marine primary producers, as the sea ice reflected most of the

391   solar shortwave radiation back to space and was therefore not favorable for the growth of phytoplankton in early spring. The

392   relatively low *Chl-a* in April 2020 was accompanied by the occurrence of abnormally low SST. In general, the relatively low

393   SST is detrimental to the melting of sea ice, which reduces the absorption of radiation by the upper ocean and weakens

394   photosynthetic activity (Brown et al., 2011). However, there is no significant correlation between *Chl-a* and SST in the BGS.

395   This may be due to the complex interactions between SST, SIC and *Chl-a*, which together affect the changes in *Chl-a* (Arrigo

396   and van Dijken, 2015; Siswanto, 2020). And the effect of a single SST on *Chl-a* may be limited. Compared to the 2005–2020

397   average, *Chl-a* in 2020 started to reveal positive anomalies in May and persisted to June (Figure 9). This implies that the

398   conditions in later spring 2020 were well suited for the growth of marine primary producers in the BGS. It was likely because

399   1) the high ice coverage in early spring was conducive to phytoplankton seeding, and 2) the low primary producers in early

400   spring were beneficial to the residue of marine nutrients. Seasonally, the *Chl-a* in the BGS reached its peak in May–June of

401   the year, one month later than the peak of SIA, which can be considered normal compared to previous observations (e.g.,

402   Dalpadado et al., 2020; Siswanto, 2020). Thereby, the impact of the abnormally large SIA in winter 2020 on spring *Chl-a* was

403   mainly limited to April 2020. Thus, the abnormal Arctic sea ice flow plays an identifiable role in regulating the seasonal timing

404   of the BGS ecosystem.
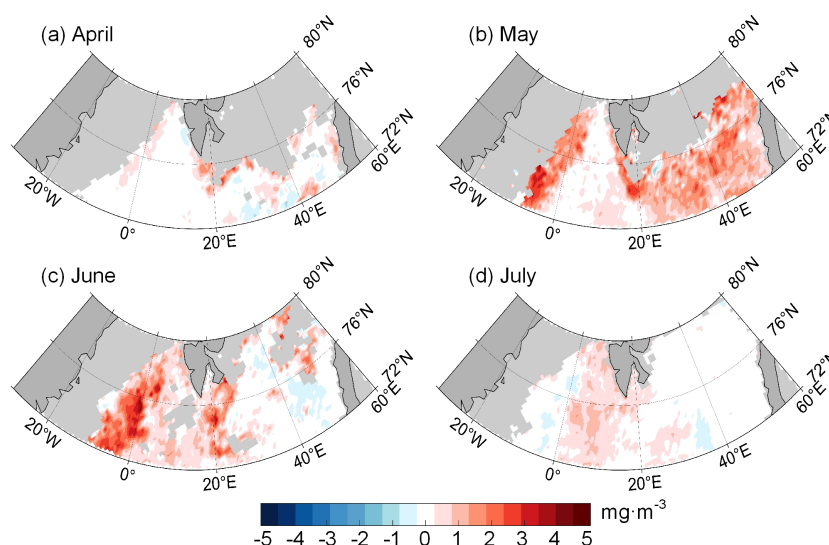
Figure 9. Monthly *Chlorophyll-a* (*Chl-a*) anomalies in the Barents and Greenland Seas from April to July 2020 compared to 2005–2020 average.

4.3 Are the anomalies and their connections identified in winter–spring 2020 typical in climatology?

409   In the past decade, positive anomalies in the winter–spring SIAF through the three defined passageways relative to the

410   1988–2020 climatology were also identified in 2011, 2017, and 2019, close to the value in 2020 (Figure 3). Therefore, we also

411   quantified the anomalies of sea ice and ocean conditions in the BGS for these years, so as to assess the representativeness of

412   the seasonal feedback mechanisms identified in winter–spring 2020 under the scenario of abnormally high Arctic sea ice

413   outflow. During these three years, the sea ice backward trajectories reconstructed starting since 30 April, 31 May, and 30 June

414   were also characterized as longer and farther west compared to 1988–2020 climatology. This suggests that the ice speeds along

415   the TPD were relatively large and could partially contribute to the positive SIAF anomalies in these years. In the BGS, although

416   small negative SIA anomalies were observed in March–June 2011, 2017, and 2019 compared to the 1979–2020 climatology,

417   their values were still much higher than those estimated from the long-term linear decreasing trends since 1979 by 0.16×10^4–

418   2.79×10^4, 0.43×10^5–1.38×10^5 and 0.66×10^5–1.06×10^5 km^2, respectively. During these three years, similar upward anomalies

419   in accumulated net surface heat fluxes were also identified in January–March, suggesting the potential coupling mechanism

420   between sea ice coverage and surface heat budget in the BGS. However, compared to the 1979–2020 climatology, there were

421   positive air temperature anomalies in January–March 2011, 2017, and 2019, in contrast to the negative air temperature

422   anomalies in 2020. This may subsequently contribute to the relatively small negative SIA anomalies in these years than in

423   2020. The SIT anomalies were calculated only for 2017 and 2019 since satellite SIT data were not available prior to 2011, and

424   we found that the BGS also showed small positive anomalies from March to June for both years compared to the average since

425   2011. Furthermore, the sea ice anomalies in these years also had impacts on the marine hydrographical and ecological

426   conditions of the BGS in April–June. The monthly SSTs in May–June of 2011, 2017, and 2019 all maintained the 2nd–4th

427   lowest in 2010–2020. During these years, the *Chl-a* also showed relatively pronounced negative anomalies in April. By

428   comparing with these years that also experienced abnormally large Arctic sea ice outflow, it can be considered that the sea ice

429   anomalies and their connections to the marine environments in the BGS identified in winter–spring 2020 were representative.

430   However, we also expect that the influences of abnormally high Arctic sea ice outflow on the sea ice and other marine

431   conditions in the BGS will gradually weaken if the Arctic sea ice continues to thin and the northward Atlantic Ocean heat flow

432   continues to increase, because the thinner ice under the increased oceanic heat would not be conducive to the survival of sea

433   ice in the BGS.

434   **5. Conclusions and recommendations**

435   In this study, we investigated the impacts of the anomalies of atmospheric circulation and Arctic sea ice outflow in the

436   winter and spring of 2020 on the sea ice conditions in the TPD downstream region of the BGS, and then discussed the

437   connections between winter–spring sea ice anomalies and the hydrographical and ecological conditions of the BGS in the

438   subsequent months until early summer 2020.

439   Compared to the 1979–2020 climatology, the AO experienced an unusually large positive phase in January–March 2020.

440   In the context of this, the SLP structure, associated with the positive CAI induced strong northerly winds along the Atlantic

441   section of TPD, which then facilitated Arctic sea ice outflow to the BGS. In the following three months, the AO decayed to be

442   negative, while the CAI remained positive, which ensured a continuous enhanced Arctic sea ice outflow to the BGS. Therefore,

443   in January–March and June 2020, the total SIAF through three passageways north of the BGS was extremely large compared

444   to the 1988–2020 climatology, mainly through the Fram Strait, which accounts for 77.6% of the total SIAF. The variabilities

445   of seasonal accumulated SIAF in 1988–2020 through these passageways were mainly dominated by the change in SIM (R =

446   +0.86 for January–June; $P < 0.001$), and it was significantly positively correlated with AO in February, and with CAI in March

447   and April ($P < 0.05$). Under the positive phases of AO and CAI in winter and/or spring 2020, the sea ice backward trajectories

448   reaching Fram Strait were relatively longer and sloped westward compared to the 1988–2020 climatology, which reflects the

449   larger ice speed along the TPD and the orientation of the TPD favoring Arctic sea ice outflow to the BGS. This regime also

450   manifests that AO affects Arctic sea ice outflow by modifying the axis alignment of TPD, while the CAI directly affects the

451   wind forcing in the TPD region.

452   The abnormally high sea ice outflow through the Fram Strait and S-FJL in winter–spring 2020 subsequently affected the

453   SIA and SIT in the BGS in the spring and early summer of 2020. In addition, the regional low air temperature anomalies in the

454   BGS favored the survival of sea ice there. Furthermore, relatively large upward anomalies in surface heat fluxes dominated by

455   turbulent heat flux in winter 2020, continuous upward anomalies in net longwave radiation in winter and early spring 2020,

456   and upward anomalies in net shortwave radiation in later spring 2020 can also reduce ice melting in the BGS. Thus, the monthly

457   SIA in the BGS in April–May 2020 remained the first or second largest in 2010–2020, and the relatively large SIT over the

458   BGS was observed since March 2020, especially in May–June. Furthermore, sea ice anomalies in the BGS subsequently

459   influenced the hydrographical and ecological conditions in the spring and early summer of 2020. In this region, the SIA in

460   April was significantly negatively correlated with the synchronous SST, as well as that with a lag of 1–3 months. And the SST

461   in April–June 2020 was the lowest in 2005–2020. In the Greenland Sea, there was a significant negative correlation between

462   the April SIA and synchronous *Chl-a*, which implies that high SIA could weaken photosynthetic activity and inhibit

463   phytoplankton blooms in early spring. A comparison with similar scenarios with a high Arctic sea ice outflow in other years in

464   the recent decade confirmed that the relationships between sea ice anomalies and the hydrographical and ecological conditions

465   in the BGS identified in winter–spring 2020 is representative. This suggests that the winter–spring Arctic sea ice outflow could

466   be considered a predictor of the changes in the conditions of sea ice and other marine environments in the BGS in the

467   subsequent months, at least until early summer.

468   In this study, we used remote sensing retrieval products of SST and *Chl-a* to characterize the apparent hydrographical and

469   ecological status in the BGS, which is very insufficient for a thorough understanding of the dynamical coupling mechanism of

470   sea ice, ocean, and biology. Remote sensing data can only reflect seasonal variations in net primary productivity in ice-free

471   oceans, whereas changes in primary productivity of ice algae and ice-submerged phytoplankton ecosystems are still not

472   quantifiable. Thus, it would be recommended to further collect the in situ observation data of regional physical oceanography,

473   biology, and ecology, as well as biogeochemical cycles to characterize the impact mechanisms of the abnormal Arctic sea ice

474   outflow on the oceanic, ecological, and biogeochemical processes in the study region. In particular, how the seasonal evolutions

475   of ocean stratification, mixing and frontal dynamics, biological communities, and greenhouse gas fluxes between ocean and

476   atmosphere respond to and/or feedback to the changes in sea ice is a scientific focus worth of attention, associated with the

477   increased Arctic sea ice outflow into the BGS region. Further studies will build on the results presented here.

478   **Appendix A: Extra figures and tables**

479
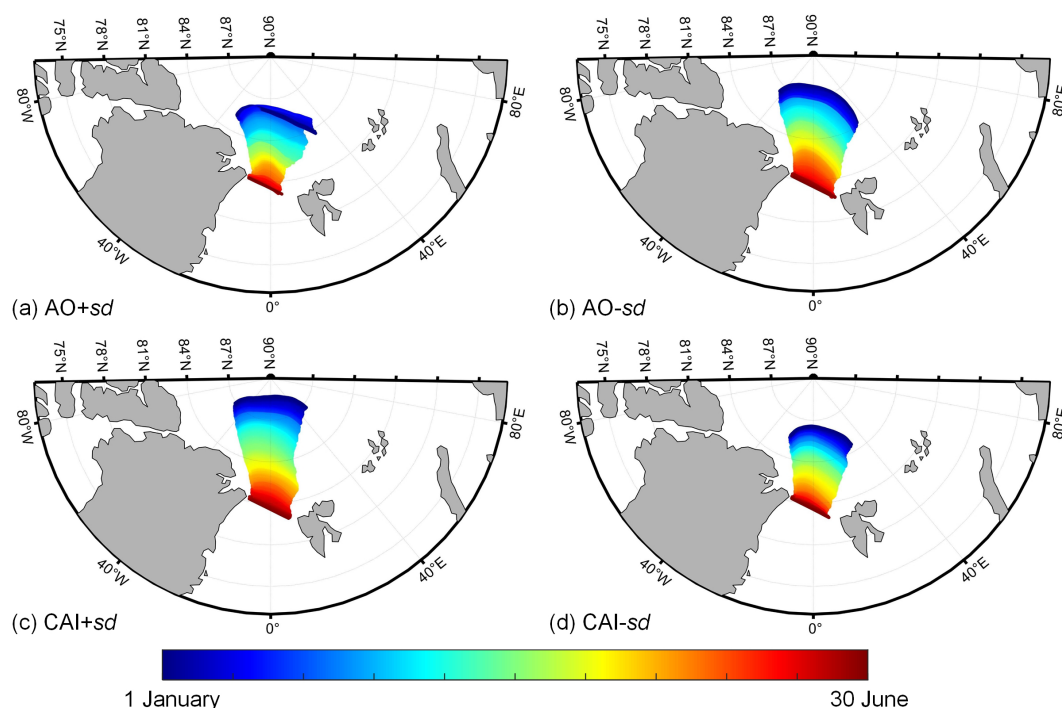
480   **Figure A1.** Sea ice backward trajectories from the Fram Strait under the extreme positive and negative phases of the Arctic Oscillation (AO)

481   and Central Arctic west-east air pressure gradient Index (CAI) in 1988–2020. Color coding of the sea ice backward trajectories denotes the

482   time from 1 January to 30 June.

483

Table A1. Correlation coefficient (R) between monthly sea ice motion speed and wind speed in the Atlantic sector of TPD for 1979–2020

Month	January	February	March	April	May	June
R	0.411**	0.355*	n.s.	0.478**	n.s.	0.493***

Note: Significance levels are $P < 0.001$ (***), $P < 0.01$ (**) and $P < 0.05$ (*); n.s. denotes nonsignificance at the 0.05 level.

Table A2. Correlation coefficient (R) between the latitude or longitude of sea ice backward trajectory endpoint from the Fram Strait and atmospheric circulation indices in 1988–2020

Investigation period	January–April	January–May	January–June
Lat *vs.* AO	n.s.	0.354*	0.347*
Lon *vs.* AO	n.s.	−0.419*	−0.514**
Lat *vs.* CAI	n.s.	0.625***	0.590***
Lon *vs.* CAI	n.s.	−0.508**	−0.599***

Note: Significance levels are $P < 0.001$ (***), $P < 0.01$ (**) and $P < 0.05$ (*); n.s. denotes nonsignificance at the 0.05 level.

Table A3. Synchronous correlation coefficient (R) between monthly sea ice area (SIA) and sea surface temperature (SST) in April, May, or June for 1982–2020.

	Month	All	North(76°–80°N)	South(72°–76°N)
	April	−0.917***	−0.764***	−0.916***
Barents Sea	May	−0.836***	−0.706***	−0.810***
	June	−0.750***	−0.677***	−0.704***
	April	−0.640***	n.s.	−0.394*
Greenland Sea	May	−0.661***	n.s.	−0.409**
	June	−0.656***	n.s.	n.s.

Note: Significance levels are $P < 0.001$ (***), $P < 0.01$ (**) and $P < 0.05$ (*); n.s. denotes nonsignificance at the 0.05 level.

The Cryosphere
Discussions
EGU
Open Access

Table A4. Lagging correlation coefficient (R) between monthly sea ice area (SIA) in April and sea surface temperature (SST) in May, June, or July for 1982–2020.

	Month	All	North(76°–80°N)	South(72°–76°N)
Barents Sea	May	−0.851***	−0.651***	−0.874***
	June	−0.752***	−0.623***	−0.739***
	July	−0.459**	−0.529***	−0.364*
Greenland Sea	May	−0.564***	n.s.	n.s.
	June	−0.446**	n.s.	n.s.
	July	n.s.	n.s.	n.s.

Note: Significance levels are $P < 0.001$ (***), $P < 0.01$ (**) and $P < 0.05$ (*); n.s. denotes nonsignificance at the 0.05 level.

Data Availability

Sea ice motion data from the NSIDC is available at https://nsidc.org/data/NSIDC-0116/versions/4 (last access on 31 Dec 2021). NSIDC sea ice concentration data is obtained from https://nsidc.org/data/G02202/versions/4 (last access on 31 Dec 2021). Sea ice area data in the Northern Hemisphere is available at https://nsidc.org/data/g02135/versions/3 (last access on Oct 2022). Sea ice thickness is downloaded from merged CryoSat-2 and SMOS (https://data.seaiceportal.de/data/cs2smos_awi/v204/; last access on 10 Apr 2022) and PIOMAS (https://pscfiles.apl.uw.edu/zhang/PIOMAS/; last access on 31 Dec 2020). Sea surface temperature data is available at https://psl.noaa.gov/data/gridded/data.noaa.oisst.v2.highres.html (last access on real-time). *Chl*-a data is obtained from https://climate.esa.int/en/projects/ocean-colour/data/ (last access on Dec 2021). The ERA5 atmospheric reanalysis data are downloaded from https://cds.climate.copernicus.eu/cdsapp#!/dataset/reanalysis-era5-single-levels (last access on real-time). The AO index is available at https://www.cpc.ncep.noaa.gov/products/precip/CWlink/daily_ao_index/ao.shtml (last access on Oct 2022).

Author Contributions

FZ carried out the analysis, processed the data, and prepared the manuscript. RL provided the concept, discussed the results, and revised the manuscript during the writing process. All authors commented on the manuscript and finalized this paper.

519   **Reference**

520   Arrigo, K.R., and van Dijken, G.L.: Continued increases in Arctic Ocean primary production, Prog. Oceanogr., 136, 60-70,
521   https://doi.org/10.1016/j.pocean.2015.05.002, 2015.

522   Bi, H., Sun, K., Zhou, X., Huang, H., and Xu, X.: Arctic Sea ice area export through the Fram Strait estimated from satellite-
523   based data: 1988–2012, IEEE. J. Stars, 9(7), 3144–3157, https://doi.org/10.1109/jstars.2016.2584539, 2016.

524   Brown, Z.W., Van Dijken, G.L., and Arrigo, K.R.: A reassessment of primary production and environmental change in the
525   Bering Sea, J. Geophys. Res. Oceans., 116(C8), https://doi.org/10.1029/2010jc006766, 2011.

526   Cai, L., Alexeev, V.A., and Walsh, J.E.: Arctic sea ice growth in response to synoptic- and large-scale atmospheric forcing from
527   CMIP5 models, J. Clim., 33(14), 6083–6099. https://doi.org/10.1175/jcli-d-19-0326.1, 2020.

528   Campbell, K., Mundy, C.J., Barber, D.G., and Gosselin, M.: Characterizing the sea ice algae chlorophyll a-snow depth
529   relationship over Arctic spring melt using transmitted irradiance, J. Marine. Syst, 147, 76–84,
530   https://doi.org/10.1016/j.jmarsys.2014.01.008, 2015.

531   Cavalieri, D.J., Gloersen, P., and Campbell, W.J.: Determination of sea ice parameters with the Nimbus 7 SMMR, J. Geophys.
532   Res. Atmospheres., 89(D4), 5355–5369, https://doi.org/10.1016/0198-0254(84)93205-9, 1984.

533   Cavalieri, D.J., and Parkinson, C.L.: Arctic sea ice variability and trends, 1979-2010, The Cryosphere, 6(4), 881–889,
534   https://doi.org/10.5194/tc-6-881-2012, 2012.

535   Comiso, J.C.: Characteristics of Arctic winter sea ice from satellite multispectral microwave observations, J. Geophys. Res.
536   Oceans., 91(C1), 975–994, https://doi.org/10.1029/jc091ic01p00975, 1986.

537   Dalpadado, P., Arrigo, K.R., van Dijken, G.L., Skjoldal, H.R., Bagøien, E., Dolgov, A.V., Prokopchuk, I.P., and Sperfeld, E.:
538   Climate effects on temporal and spatial dynamics of phytoplankton and zooplankton in the Barents Sea, Prog. Oceanogr.,
539   185, 102320, https://doi.org/10.1016/j.pocean.2020.102320, 2020.

540   de Steur, L., Hansen, E., Mauritzen, C., Beszczynska-Moeller, A., and Fahrbach, E.: Impact of recirculation on the East
541   Greenland Current in Fram Strait: Results from moored current meter measurements between 1997 and 2009, Deep-Sea
542   Research Part I-Oceanographic Research Papers, 92, 26–40, https://doi.org/10.1016/j.dsr.2014.05.018, 2014.

543   Dethloff, K., Maslowski, W., Hendricks, S., Lee, Y.J., Goessling, H.F., Krumpen, T., Haas, C., Handorf, D., Ricker, R., and
544   Bessonov, V.: Arctic sea ice anomalies during the MOSAiC winter 2019/20, The Cryosphere, 16(3), 981–1005,
545   https://doi.org/10.5194/tc-16-981-2022, 2022.

546   Dorr, J., Arthun, M., Eldevik, T., and Madonna, E.: Mechanisms of regional winter sea-ice variability in a warming Arctic, J.
547   Clim., 34(21), 8635–8653, https://doi.org/10.1175/jcli-d-21-0149.1, 2021.

548   Frey, K.E., Moore, G.W.K., Cooper, L.W., and Grebmeier, J.M.: Divergent patterns of recent sea ice cover across the Bering,
549   Chukchi,   and   Beaufort   seas   of   the   Pacific   Arctic   Region,   Prog.   Oceanogr.,   136,   32-49,
550   https://doi.org/10.1016/j.pocean.2015.05.009, 2015.

551   Fetterer, F., Knowles, K., Meier, W.N., Savoie, M., and Windnagel, A.K.: Sea Ice Index, Version 3. Boulder, Colorado USA,
552   National Snow and Ice Data Center, https://doi.org/10.7265/N5K072F8, 2017.

553   Graham, R.M., Hudson, S.R., and Maturilli, M.: Improved performance of ERA5 in Arctic gateway relative to four global
554   atmospheric reanalyses, Geophys. Res. Lett., 46(11), 6138–6147, https://doi.org/10.1029/2019gl082781, 2019.

555   Hersbach, H., Bell, B., Berrisford, P., Hirahara, S., Horanyi, A., Munoz-Sabater, J., Nicolas, J., Peubey, C., Radu, R., Schepers,
556   D., Simmons, A., Soci, C., Abdalla, S., Abellan, X., Balsamo, G., Bechtold, P., Biavati, G., Bidlot, J., Bonavita, M., De
557   Chiara, G., Dahlgren, P., Dee, D., Diamantakis, M., Dragani, R., Flemming, J., Forbes, R., Fuentes, M., Geer, A.,
558   Haimberger, L., Healy, S., Hogan, R.J., Holm, E., Janiskova, M., Keeley, S., Laloyaux, P., Lopez, P., Lupu, C., Radnoti,
559   G., de Rosnay, P., Rozum, I., Vamborg, F., Villaume, S., and Thepaut, J.N.: The ERA5 global reanalysis, Q. J. Roy. Meteor.
560   Soc., 146(730), 1999–2049, https://doi.org/10.1002/qj.3803, 2020.

561   Krumpen, T., Birrien, F., Kauker, F., Rackow, T., von Albedyll, L., Angelopoulos, M., Belter, H. J., Bessonov, V., Damm, E.,
562   Dethloff, K., Haapala, J., Haas, C., Harris, C., Hendricks, S., Hoelemann, J., Hoppmann, M., Kaleschke, L., Karcher,
563   M., Kolabutin, N., Lei, R., Lenz, J., Morgenstern, A., Nicolaus, M., Nixdorf, U., Petrovsky, T., Rabe, B., Rabenstein, L.,
564   Rex, M., Ricker, R., Rohde, J., Shimanchuk, E., Singha, S., Smolyanitsky, V., Sokolov, V., Stanton, T., Timofeeva, A.,
565   Tsamados, M., and Watkins, D.: The MOSAiC ice floe: Sediment-laden survivor from the Siberian shelf, The
566   Cryosphere, 14(7), 2173–2187, http://dx.doi.org/10.5194/tc-14-2173-2020, 2020.

567   Krumpen, T., von Albedyll, L., Goessling, H.F., Hendricks, S., Juhls, B., Spreen, G., Willmes, S., Belter, H.J., Dethloff, K.,
568   Haas, C., Kaleschke, L., Katlein, C., Tian-Kunze, X., Ricker, R., Rostosky, P., Rueckert, J., Singha, S., and Sokolova, J.:
569   MOSAiC drift expedition from October 2019 to July 2020: sea ice conditions from space and comparison with previous
570   years, The Cryosphere, 15(8), 3897–3920, https://doi.org/10.5194/tc-15-3897-2021, 2021.

571   Kwok, R.: Outflow of Arctic ocean sea ice into the Greenland and Barents Seas: 1979–2007, J. Clim., 22(9), 2438–2457,
572   https://doi.org/10.1175/2008jcli2819.1, 2009.

573   Kwok, R., Cunningham, G., Wensnahan, M., Rigor, I., Zwally, H., and Yi, D.: Thinning and volume loss of the Arctic Ocean
574   sea ice cover: 2003–2008, J. Geophys. Res. Oceans., 114(C7), https://doi.org/10.1029/2009jc005312, 2009.

575   Lei, R., Gui, D., Hutchings, J.K., Wang, J., and Pang, X.: Backward and forward drift trajectories of sea ice in the northwestern
576   Arctic   Ocean   in   response   to   changing   atmospheric   circulation,   Int.   J.   Climatol.,   39(11),   4372–4391,
577   https://doi.org/10.1002/joc.6080, 2019.

578   Lei, R., Heil, P., Wang, J., Zhang, Z., Li, Q., and Li, N.: Characterization of sea-ice kinematic in the Arctic outflow region

579   using buoy data, Polar. Res., 35(1), https://doi.org/10.3402/polar.v35.22658, 2016.

580   Lemke, P., Harder, M., and Hilmer, M.: The response of arctic sea ice to global change, Clim. Change., 46(3), 277–287,
581   https://doi.org/10.1023/a:1005695109752, 2000.

582   Lind, S., Ingvaldsen, R.B., and Furevik, T.: Arctic warming hotspot in the northern Barents Sea linked to declining sea-ice
583   import. Nat. Clim. Change., 8(7), 634–639, https://doi.org/10.1038/s41558-018-0205-y, 2018.

584   Mayot, N., Matrai, P.A., Arjona, A., Belanger, S., Marchese, C., Jaegler, T., Ardyna, M., and Steele, M.: Springtime export of
585   Arctic sea ice influences phytoplankton production in the Greenland Sea, J. Geophys. Res. Oceans., 125(3),
586   https://doi.org/10.1029/2019jc015799, 2020.

587   Meier, W.N., Fetterer, F., Windnagel, A.K., and Stewart, J.S.: NOAA/NSIDC Climate Data Record of Passive Microwave Sea
588   Ice Concentration, Version 4, Boulder, Colorado USA. NSIDC: National Snow and Ice Data Center,
589   https://doi.org/10.7265/efmz-2t65, 2021.

590   Minnett, P.J., and Key, E.L.: Meteorology and atmosphere–surface coupling in and around polynyas, Elsevier Oceanography
591   Series, 74, 127–161, https://doi.org/10.1016/S0422-9894(06)74004-1, 2007.

592   Mori, M., Watanabe, M., Shiogama, H., Inoue, J., and Kimoto, M.: Robust Arctic sea-ice influence on the frequent Eurasian
593   cold winters in past decades, Nat. Geosci., 7(12), 869–873, https://doi.org/10.1038/ngeo2277, 2014.

594   Mørk, T., Bohlin, J., Fuglei, E., Asbakk, K., and Tryland, M.: Rabies in the arctic fox population, Svalbard, Norway, J. Wildlife.
595   Dis., 47(4), 945–957, https://doi.org/10.7589/0090-3558-47.4.945, 2011.

596   Nicolaus, M., Riemann-Campe, K., Hutchings, J.K., Granskog, M.A., Krishfield, R., Lei, R., Li, T., and Rabe, B.: Drift
597   trajectories of the main sites of the Distributed Network and the Central Observatories of MOSAiC 2019/2020, Epic,
598   2021.

599   Onarheim, I.H., Eldevik, T., Smedsrud, L.H., and Stroeve, J.C.: Seasonal and regional manifestation of Arctic sea ice loss, J.
600   Clim., 31(12), 4917–4932, https://doi.org/10.1175/jcli-d-17-0427.1, 2018.

601   Parkinson, C.L., and Washington, W.M.: A large-scale numerical model of sea ice, J. Geophys. Res. Oceans., 84(C1), 311–337,
602   https://doi.org/10.1029/JC084iC01p00311, 1979.

603   Peeken, I., Primpke, S., Beyer, B., Gutermann, J., Katlein, C., Krumpen, T., Bergmann, M., Hehemann, L., and Gerdts, G.:
604   Arctic sea ice is an important temporal sink and means of transport for microplastic, Nat. Commun., 9,
605   https://doi.org/10.1038/s41467-018-03825-5, 2018.

606   Peng, G., Meier, W.N., Scott, D.J., and Savoie, M.H.: A long-term and reproducible passive microwave sea ice concentration
607   data record for climate studies and monitoring, Earth. Syst. Sci. Data., 5(2), 311–318, https://doi.org/10.5194/essd-5-311-
608   2013, 2013.

609   Previdi, M., Smith, K.L., and Polvani, L.M.: Arctic amplification of climate change: a review of underlying mechanisms,
610   Environ. Res. Lett., 16(9), https://doi.org/10.1088/1748-9326/ac1c29, 2021.

611   Reynolds, R.W., Smith, T.M., Liu, C., Chelton, D.B., Casey, K.S., and Schlax, M.G.: Daily high-resolution-blended analyses
612   for sea surface temperature, J. Clim., 20(22), 5473–5496, https://doi.org/10.1175/2007jcli1824.1, 2007.

The Cryosphere
Discussions
Open Access
EGU

613   Ricker, R., Hendricks, S., Kaleschke, L., Tian-Kunze, X., King, J., and Haas, C.: A weekly Arctic sea-ice thickness data record
614   from merged CryoSat-2 and SMOS satellite data, The Cryosphere, 11(4), 1607–1623, https://doi.org/10.5194/tc-11-1607-
615   2017, 2017.

616   Ricker, R., Kauker, F., Schweiger, A., Hendricks, S., Zhang, J., and Paul, S.: Evidence for an increasing role of ocean heat in
617   Arctic winter sea ice growth, J. Clim., 34(13), 5215–5227, https://doi.org/10.1175/jcli-d-20-0848.1, 2021.

618   Rigor, I.G., Wallace, J.M., and Colony, R.L.: Response of sea ice to the Arctic Oscillation, J. Clim., 15(18), 2648–2663,
619   https://doi.org/10.1029/1999gl002389, 2002.

620   Sathyendranath, S., Jackson, T., Brockmann, C., Brotas, V., Calton, B., Chuprin, A., Clements, O., Cipollini, P., Danne, O.,
621   Dingle, J., Donlon, C., Grant, M., Groom, S., Krasemann, H., Lavender, S., Mazeran, C., Melin, F., Muller, D., Steinmetz,
622   F., Valente, A., Zuhlke, M., Feldman, G., Franz, B., Frouin, R., Werdell, J., and Platt, T.: ESA Ocean Colour Climate
623   Change   Initiative   (Ocean_Colour_cci):   Version   5.0   Data,   Centre   for   Environmental   Data   Analysis,
624   https://doi.org/10.5285/1dbe7a109c0244aaad713e078fd3059a, 2021.

625   Schlichtholz, P.: Subsurface ocean flywheel of coupled climate variability in the Barents Sea hotspot of global warming, Sci.
626   Rep., 9(1), 1–16, https://doi.org/10.1038/s41598-019-49965-6, 2019.

627   Schweiger, A., Lindsay, R., Zhang, J.L., Steele, M., Stern, H., and Kwok, R.: Uncertainty in modeled Arctic sea ice volume, J.
628   Geophys. Res. Oceans., 116(C8), https://doi.org/10.1029/2011jc007084, 2011.

629   Shu, Q., Wang, Q., Song,, Z., and Qiao, F.: The poleward enhanced Arctic Ocean cooling machine in a warming climate, Nat.
630   Commun., 12(1), https://doi.org/10.1038/s41467-021-23321-7, 2021.

631   Siswanto, E.: Temporal variability of satellite-retrieved chlorophyll-a data in Arctic and subarctic ocean regions within the past
632   two decades, Int. J. Remote. Sens., 41(19), 7427–7445, https://doi.org/10.1080/01431161.2020.1759842, 2020.

633   Smedsrud, L.H., Esau, I., Ingvaldsen, R.B., Eldevik, T., Haugan, P.M., Li, C., Lien, V.S., Olsen, A., Omar, A.M., and Otterå,
634   O.H.: The role of the Barents Sea in the Arctic climate system, Rev. Geophy. , 51(3), 415–449,
635   https://doi.org/10.1017/cbo9780511535888.008, 2013.

636   Smedsrud, L.H., Halvorsen, M.H., Stroeve, J.C., Zhang, R., and Kloster, K.: Fram Strait sea ice export variability and
637   September Arctic sea ice extent over the last 80 years, The Cryosphere, 11(1): 65–79, https://doi.org/10.5194/tc-11-65-
638   2017, 2017.

639   Spreen, G., Kern, S., Stammer, D., and Hansen, E.: Fram Strait sea ice volume export estimated between 2003 and 2008 from
640   satellite data, Geophys. Res. Lett., 36(19), https://doi.org/10.1029/2009GL039591, 2009.

641   Stroeve, J., Barrett, A., Serreze, M., and Schweiger, A.: Using records from submarine, aircraft and satellites to evaluate climate
642   model simulations of Arctic sea ice thickness, The Cryosphere, 8(5), 1839–1854, https://doi.org/10.5194/tc-8-1839-2014,
643   2014.

644   Thompson, D.W.J., and Wallace, J.M. : The Arctic Oscillation signature in the wintertime geopotential height and temperature
645   fields, Geophys. Res. Lett., 25(9), 1297–1300, https://doi.org/10.1029/98gl00950, 1998.

646   Tschudi, M.A,, Meier, W.N., Stewart, J.S., Fowler, C., and Maslanik, J.: Polar Pathfinder Daily 25 km EASE-Grid Sea Ice
647   Motion Vectors, Version 4, Boulder, Colorado USA, NASA National Snow and Ice Data Center Distributed Active

648   Archive Center, https://doi.org/10.5067/INAWUWO7QH7B, 2019.

649   Tschudi, M.A., Meier, W.N., and Stewart, J.S.: An enhancement to sea ice motion and age products at the National Snow and
650   Ice Data Center (NSIDC), The Cryosphere, 14(5), 1519–1536, https://doi.org/10.5194/tc-14-1519-2020, 2020.

651   Vihma, T., Tisler, P., and Uotila, P.: Atmospheric forcing on the drift of Arctic sea ice in 1989–2009, Geophys. Res. Lett., 39(2),
652   https://doi.org/10.1029/2011gl050118, 2012.

653   Wang, X., Key, J., Kwok, R., and Zhang, J.: Comparison of Arctic sea ice thickness from satellites, aircraft, and PIOMAS data,
654   Remote Sens., 8(9), https://doi.org/10.3390/rs8090713, 2016.

655   Wang, Y., Bi, H., Huang, H., Liu, Y., Liu, Y., Liang, X., Fu, M., and Zhang, Z.: Satellite-observed trends in the Arctic sea ice
656   concentration for the period 1979–2016, J. Oceanol. Limnol., 37(1), 18–37, https://doi.org/10.1007/s00343-019-7284-0,
657   2019.

658   Wassmann, P., Slagstad, D., and Ellingsen, I.: Primary production and climatic variability in the European sector of the Arctic
659   Ocean prior to 2007: preliminary results, Polar. Biol., 33(12), 1641–1650, https://doi.org/10.1007/s00300-010-0839-3,
660   2010.

661   Zhang, F., Pang, X., Lei, R., Zhai, M., Zhao, X., and Cai, Q.: Arctic sea ice motion change and response to atmospheric forcing
662   between 1979 and 2019, Int. J. Climatol. , 42(3), 1854–1876, https://doi.org/10.1002/joc.7340, 2022.

663   Zhang, J. and Rothrock, D.A.: Modeling global sea ice with a thickness and enthalpy distribution model in generalized
664   curvilinear   coordinates,   Mon.   Weather.   Rev.,   131(5),   845–861,   https://doi.org/10.1175/1520-
665   0493(2003)131<0845:mgsiwa>2.0.co;2, 2003.